

# Visualizing the Local Atomic Environment Features of Machine Learning

## Interatomic Potential

Xuqiang Shao<sup>a</sup>, Yuqi Zhang<sup>a</sup>, Di Zhang<sup>b</sup>, Tianxiang Gao<sup>c</sup>, Xinyuan Liu<sup>c</sup>, Zhiran Gan<sup>c</sup>, Fanshun Meng<sup>d</sup>, Hao Li<sup>b\*</sup>, Weijie Yang<sup>c\*</sup>

<sup>a</sup> School of Control and Computer Engineering, North China Electric Power University, Baoding 071003, China

<sup>b</sup> Advanced Institute for Materials Research (WPI-AIMR), Tohoku University, Sendai 980-8577, Japan

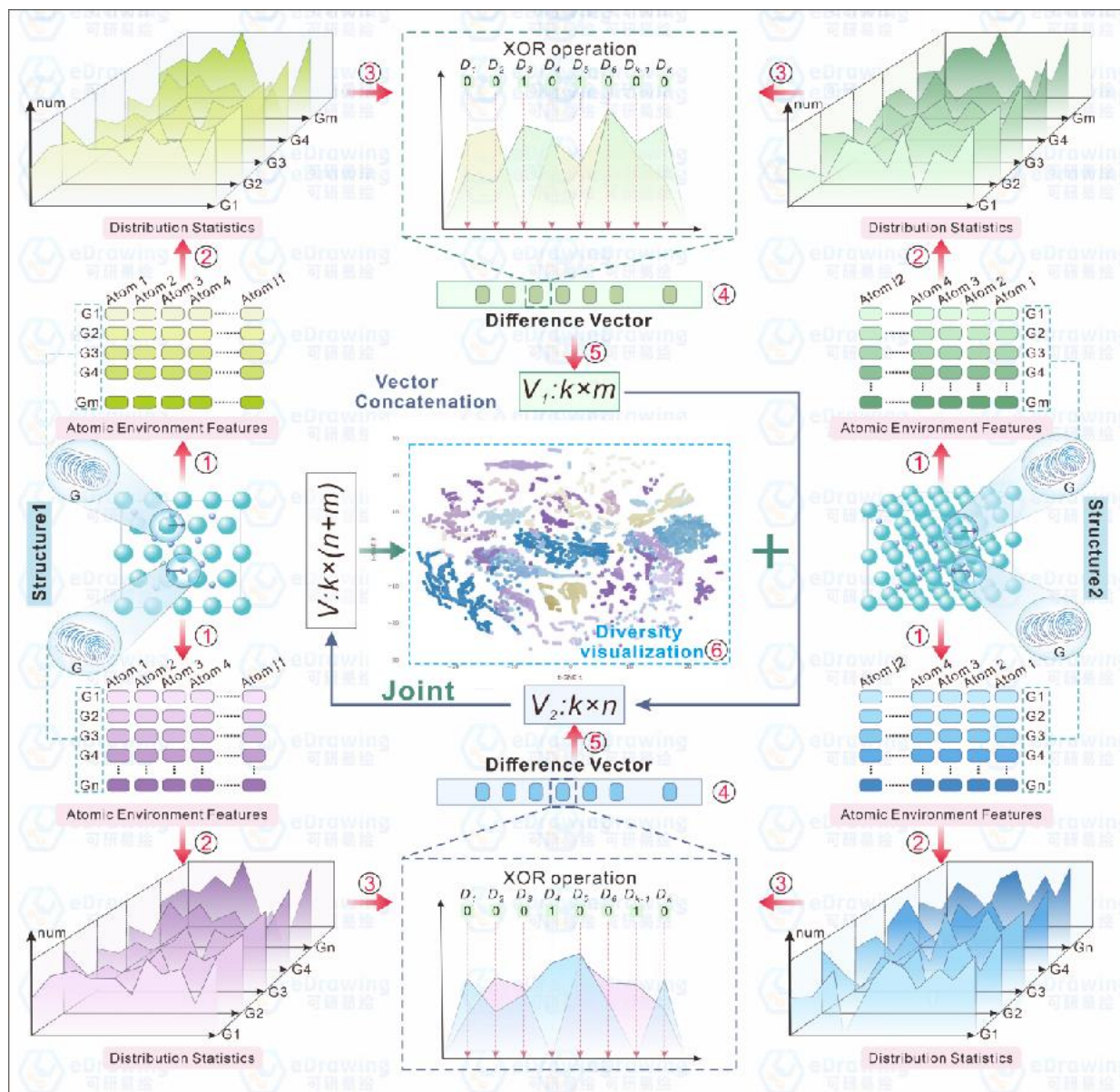
<sup>c</sup> Department of Power Engineering, School of Energy and Power Engineering, North China Electric Power University, Baoding, 071003, Hebei, China

<sup>d</sup> School of Science, Liaoning University of Technology, Jinzhou, 121001, China

## Abstract

This paper addresses the challenges of creating efficient and high-quality datasets for machine learning potential functions. We present a novel approach, termed DV-LAE (Difference Vectors based on Local Atomic Environments), which utilizes the properties of atomic local environments and employs histogram statistics to generate difference vectors. This technique facilitates dataset screening and optimization, effectively minimizing redundancy while maintaining data diversity. We have validated the optimized datasets in high-temperature and high-pressure hydrogen systems as well as the  $\alpha$ -Fe/H binary system, demonstrating a significant reduction in computational resource usage without compromising prediction accuracy. Additionally, our method has revealed new structures that emerge during simulations but were underrepresented in the initial training datasets. The redundancy in the datasets and the distribution of these new structures can be visually analyzed through the visualization of difference vectors. This approach enhances our understanding of the characteristics of these newly formed structures and their impact on physical processes.

**Keywords:** Machine-learning Potential, Local Atomic Environment Description.



**Graphical Abstract**

## 1. Introduction

In the cutting-edge research of modern materials science and chemical physics, first-principles calculation, with its theoretical rigor, provides a solid basis for revealing the physical and chemical properties at the atomic scale, and becomes an indispensable tool for understanding and designing new materials.<sup>1-4</sup> However, these methods based on quantum mechanics, such as density functional theory (DFT), while accurate, are limited by high computational costs, especially for complex systems containing a large number of atoms and long-term dynamic simulations, which significantly limit their application.<sup>5-7</sup> It is in this context that machine learning potential functions (MLPs) came into being. By learning the reference data obtained from first-principles calculations, they reconstruct the interatomic potential energy surface with high efficiency

and near-first-principles accuracy, greatly widening the space-time scale of the simulation, and thus showing extraordinary potential in understanding chemical reaction mechanisms, phase transition processes, and material property prediction.<sup>8–13</sup>

The development of MLPs is an intricate endeavor, predominantly contingent upon two pivotal components: the design of the machine learning model and the construction of the dataset. Collectively, these elements dictate the ultimate performance, precision, and generalizability of the model.<sup>14–16</sup> An adeptly crafted machine learning model is essential for the efficacious capture and articulation of the underlying physical laws. In the construction of deep neural network models, a series of critical requirements must be met, which are not limited to the model having an appropriate functional form, maintaining symmetry, and possessing good scalability.<sup>17,18</sup> The meticulous design of the model architecture, including the number of layers, the number of nodes, and the selection of activation functions, is crucial for determining the model's complexity, training efficiency, and its ability to fit complex potential energy surfaces (PES).<sup>19,20</sup> These characteristics collectively ensure that the model can accurately predict the interactions and potential energy under different atomic structures.

Despite the plethora of research dedicated to the refinement of machine learning models, culminating in the emergence of various high-performance network models, such as the ANI<sup>21</sup> model grounded in DNNs, the SchNet<sup>22</sup> model leveraging convolutional neural networks, and the GNNFF<sup>23</sup> model utilizing graph neural networks, the dataset construction remains a crucial component. In the absence of a high-quality dataset, even the most sophisticated models are impeded from realizing their full potential. The construction of a dataset is the linchpin in ensuring the model's generalizability. In the context of PES modeling, this typically necessitates the assembly or simulation of a vast array of atomic configurations that encapsulate the myriad states the system may inhabit, alongside the acquisition of their corresponding energies and forces. An ideal dataset ought to span the entire phase space of the system, guaranteeing that the model learns all the pivotal physical characteristics during the training process. Should the dataset be deficient or biased, the model may succumb to overfitting to specific patterns within the data, thereby significantly undermining its predictive accuracy in previously unseen scenarios.<sup>24–26</sup>

In contemporary materials science research, molecular dynamics (MD) and Monte Carlo (MC) simulations have become important means of rapidly generating structured data sets.<sup>27–33</sup> These computational simulation techniques provide rich data resources for the training of machine learning models, especially in the era of big data, where publicly available material databases greatly expand the scale and diversity of available data.<sup>34–38</sup> However, although the surge in data volume provides a broader space for model training, it also raises many challenges. In practice, it is not practical to use all data for training, so it is crucial to

accurately select the structural data that meets the research objectives.

Although the traditional manual screening method can be integrated into the in-depth understanding of experts, it has several inherent limitations. First, the manual screening process is not only time consuming but also expensive, especially when dealing with large data sets. Secondly, the method is susceptible to subjective judgment, which may lead to selection bias and inconsistency of results. More critically, manual filtering may not be able to fully cover the entire data set, thus making full use of data resources. Additionally, the use of PCA for dimensionality reduction, a common approach in data preprocessing, has its own set of disadvantages. PCA, while effective in capturing global patterns, often overlooks local structural nuances that are critical for material science applications. It tends to smooth over the subtle variations that could be pivotal for understanding complex material behaviors, leading to a loss of critical information and potentially misleading interpretations..

In order to break through the bottleneck of traditional data screening, researchers are gradually adopting active learning strategies such as DP-GEN.<sup>39,40</sup> The DP-GEN framework combines the advantages of differentiable programming and genetic algorithm, and intelligently guides the selection of data samples through the real-time evaluation of learning progress by the model. This strategy not only significantly reduces the reliance on manual labeling, but also improves the efficiency and accuracy of the screening process. DP-GEN fine-tunes genetic algorithm parameters through gradient optimization, enabling efficient search and precise optimization in material discovery. However, the computational cost of the DP-GEN iterative optimization process is relatively high. Therefore, how to effectively mine and apply high-quality data in large data sets at low cost remains an important and urgent challenge in the field.

In this study, we develop an innovative method to construct structural difference vectors by integrating features and descriptors of the local atomic environment using histogram statistics. These vectors were reduced and visualized by t-SNE algorithm, and then the data set was screened and optimized. This method not only significantly reduces the redundancy of the data set, but also maintains the diversity of the data, thus effectively improving the training efficiency of MLPs without sacrificing the generalization ability of the model. This method has demonstrated excellent performance in hydrogen systems under high temperature and pressure and  $\alpha$ -Fe/H two-element systems. The optimization of the data set not only reduces the dependence on computing resources, but also ensures the accuracy of the model predictions. In particular, in the graphene growth simulation, visual analysis of difference vectors revealed similarities between new structures formed at specific incident kinetic energy and known structures, providing new insights into the fundamental mechanisms of material growth.

## Results and Discussion

### 2.1 Difference Vector Construction and Nonlinear Dimensionality Reduction for Capturing Local Structural Features

While exploring dimensionality reduction in high-dimensional data, PCA (Principal Component Analysis) stands as a classic linear dimensionality reduction technique. Although it effectively extracts overall numerical features of the data, it has limitations when dealing with local subtle differences and structural features. While exploring dimensionality reduction in high-dimensional data, PCA (Principal Component Analysis) stands as a classic linear dimensionality reduction technique. Although it effectively extracts overall numerical features of the data, it has limitations when dealing with local subtle differences and structural features.

To overcome this challenge, we propose a difference vector construction method based on histogram statistics that can effectively capture subtle differences between local environments and better preserve structural diversity during dimensionality reduction. Through histogram statistics, we are able to construct difference vectors reflecting actual differences among different structures, which not only reduces redundant data but also alleviates PCA's shortcomings in handling local structure to some extent. The difference vector approach emphasizes local relationships without requiring global structure retention, making the reduced-dimensional data more intuitively reflect the actual relationship between data points.

We combine the difference vector method with nonlinear dimensionality reduction techniques such as t-SNE to achieve more intuitive and interpretable structural differences visualization. As a non-linear dimensionality reduction technique, t-SNE focuses on preserving local structure between points in high-dimensional data by optimizing Kullback-Leibler divergence (KL divergence), keeping nearby points close together in low-dimensional space. Compared to PCA, t-SNE pays more attention to retaining local structures rather than global ones, making it unique advantages for data visualization and pattern discovery.

## 2.2 Visualization of AIMD Trajectories and Carbon Dataset Configurations

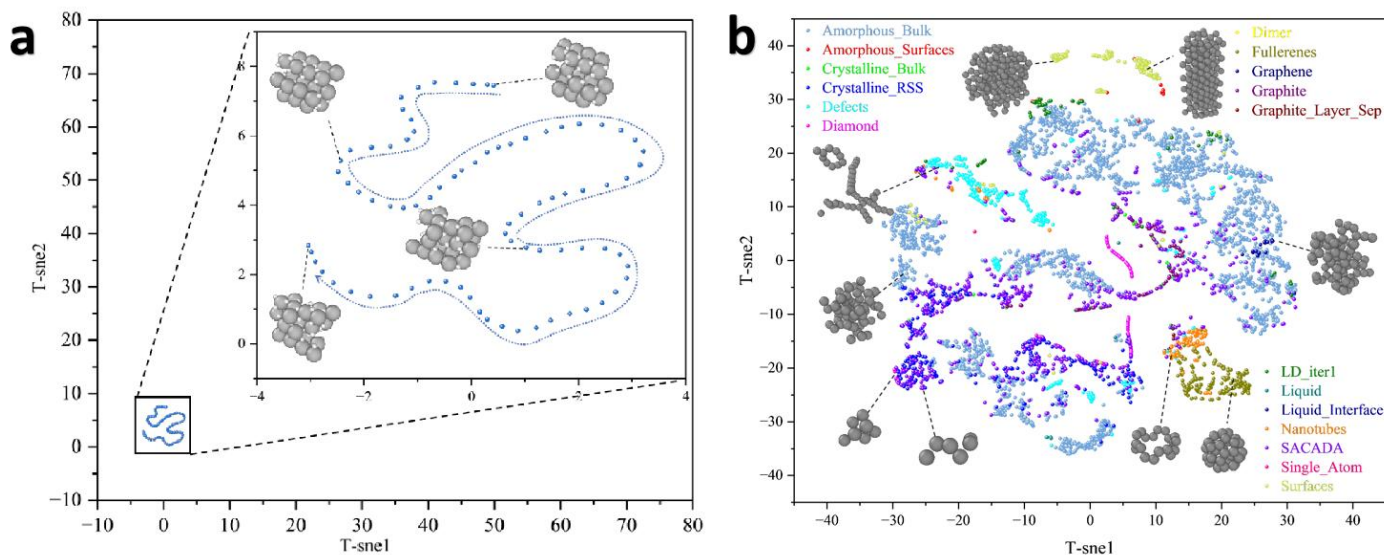


**Figure 1(a)** the visualization displays the AIMD (Ab Initio Molecular Dynamics) trajectory of gaseous hydrogen atoms. The hydrogen atoms are represented by grey spheres, and their dynamic movement over time is depicted by the blue dotted lines, which trace the atomic trajectories. (b) the visualization of a dataset related to carbon structures. Different colors represent various configurations and forms of carbon atoms.

**Figure 1** presents two visualizations demonstrating different atomic configurations. In **Figure 1a**, we visualize the AIMD (Ab Initio Molecular Dynamics) trajectory of gaseous hydrogen atoms, simulated under the condition of  $\text{MgH}_2$  at 700 K. The grey spheres represent individual hydrogen atoms, and their movement over time is depicted by blue dotted lines, illustrating the atomic trajectories. During the simulated time frame, the hydrogen structures remain relatively consistent, leading to the trajectory points being closely grouped, a feature highlighted by the zoomed-in section of the image. This suggests that the atomic configurations do not deviate significantly under these conditions, maintaining a localized, cohesive structure.

**Figure 1b** provides a t-SNE visualization of a diverse dataset related to carbon atomic structures. Each color represents a different atomic configuration of carbon, from well-characterized structures such as diamond and graphite to more complex forms like defects, surfaces, and nanotubes. The wide distribution of light blue points corresponds to block structures, indicating their broad presence across different regions of the dataset. This comprehensive distribution highlights the versatility of carbon in adopting a variety of bonding environments and molecular geometries. The distinct clustering of atomic configurations within the space further emphasizes the diversity in carbon's structural forms and provides valuable insights into the relationships between these various configurations.

## 2.3 High Temperature and High-Pressure Hydrogen System

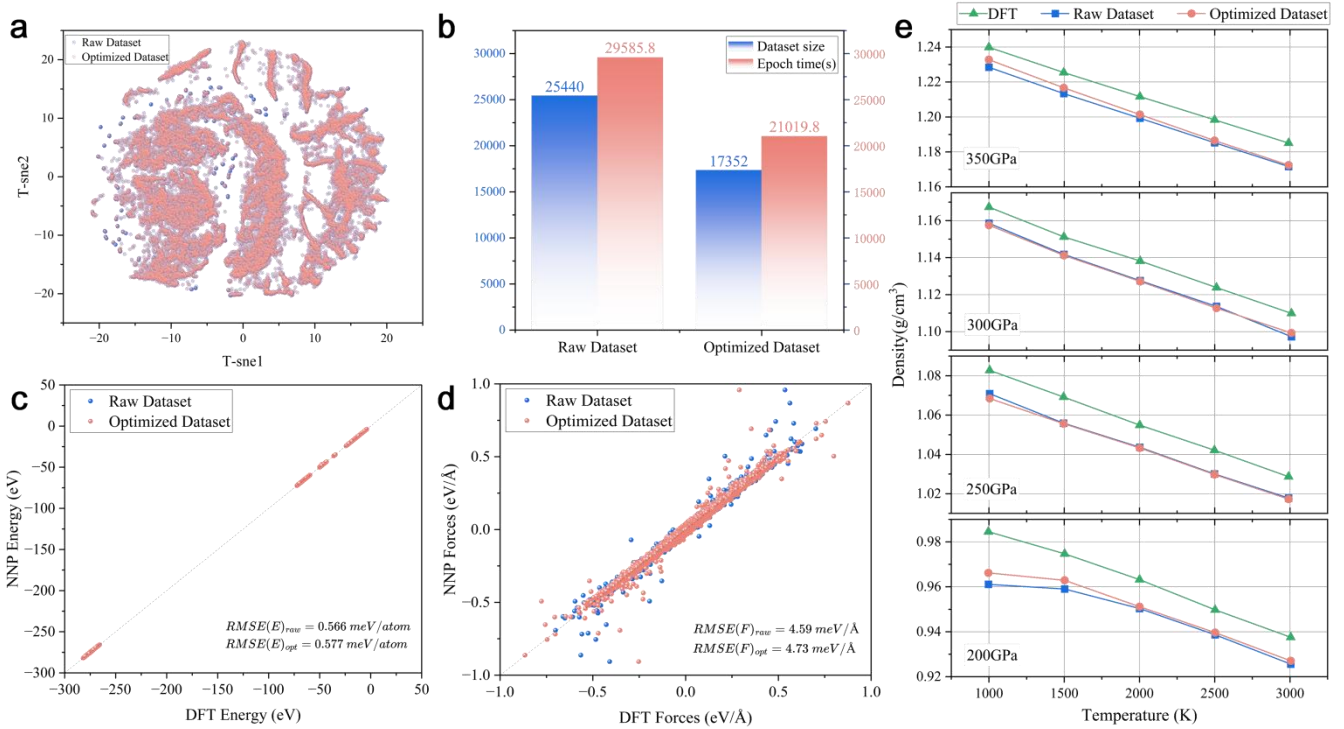


**Figure 2**(a) t-SNE visualization of the high-temperature, high-pressure hydrogen system dataset, highlighting structural overlaps and redundancy. The blue ball represents the original dataset, and the red ball represents the optimized dataset. (b) Comparison of the average training time per iteration for the original dataset (25,440 structures) and the optimized dataset (17,352 structures). (c & d) Training results comparison: Energy RMSE for the full dataset is 0.566 meV/atom and for the optimized subset is 0.577 meV/atom. Force RMSE for the full dataset is 4.59 meV/Å, and for the optimized subset is 4.73 meV/Å. (e) Comparison of density isoclines predicted by the machine learning potential function. The green triangles represent standard reference data, while the blue squares and red circles represent predictions from the potential functions trained on the original dataset and the optimized dataset, respectively. Both datasets show similar accuracy.

We utilized the training dataset from literature <sup>41</sup>, which encompasses a total of 25,440 structural configurations of the high-temperature, high-pressure hydrogen system. This choice allows us to specifically evaluate the effectiveness of our method for systems with a single type of atom, providing valuable insights into its applicability and potential limitations. By constructing difference vectors and subsequently applying t-SNE for visualization purposes, we achieved a graphical representation of the dataset's diversity as illustrated in **Figure 2a**. In the darker areas, it indicates that there are multiple data that are very close or overlapping. Through the analysis here, a considerable number of structural overlaps are revealed, which implies data redundancy.

Leveraging the outcomes of the visualization, we executed a targeted data screening. Consequently, we established an optimized subset comprising 17,352 structures, signifying a reduction in data volume by approximately 31.79%. **Figure 2b** illustrates the comparison of the average training time per iteration between the original and optimized datasets. The average training time per iteration decreased from 29,585.8 seconds to 21,018.9 seconds, resulting in a remarkable 41.4% reduction in time cost per iteration. This optimization significantly diminished the expenses incurred during the training process.

To confirm that the optimized dataset can effectively substitute the original dataset in terms of diversity, we evaluated the prediction accuracy of energy and force using the same test set for potential functions trained on both the original and optimized datasets. **Figures 2c** and **Figures 2d** illustrate a comparative analysis of the predicted energy and force values using the machine learning potential function trained on these datasets. Each scatter plot aligns Density Functional Theory (DFT) reference values along the x-axis and the machine learning model's predictions along the y-axis. The red and blue spheres in these plots distinguish the predictions from the optimized and original datasets, respectively, facilitating a direct comparison of the model's performance. Experimental results depicted in **Figures 2c** and **Figures 2d** reveal that the machine learning potential function trained on the optimized dataset maintains comparable accuracy to the one trained on the full dataset. In terms of energy prediction, the Root Mean Square Error (RMSE) shows a slight uptick from 0.566 meV/atom to 0.577 meV/atom, indicating a mere 1.94% increase. For force prediction, the RMSE marginally increases from 4.59 meV/Å to 4.73 meV/Å, representing a 3.05% increment. Despite these slight variations in RMSE, the tangible advantages of the reduced data volume and shorter training times far outweigh these minor differences, emphasizing the efficacy and utility of the data optimization approach utilized.

In order to further verify the predictive ability of the machine learning potential function we screened the data set and trained, a series of comparative experiments covering the pressure range of 200 GPa to 350 GPa were conducted in this study using a method similar to the simulation experiment of high temperature and high pressure described in literature <sup>41</sup>. The tests were performed at 50 GPa intervals, while at each pressure point, an initial temperature from 1000 K to 3000 K was set to fully explore the effect of temperature on the hydrogen equation of state. As depicted in **Figure 2e**, the left panel illustrates the density isoclines as predicted by the machine learning potential function reported in literature <sup>41</sup>. The green triangle data in the figure represents the standard reference data, and the blue square and red circle data respectively represent the predicted values of the potential function trained by the original data set and the optimized data set. It can be seen from the figure that the predicted values of the potential function trained by the original data set

and the optimized data set have very little difference, and they are both very close to the standard data. Especially at 200GPa, the optimized data set is even closer to the reference data than the original data set. This indicates that the optimized dataset represents an excellent proxy for the original dataset in training the potential function, yielding impressive results.

## 2.4 Binary system ( $\alpha$ -Fe/H)

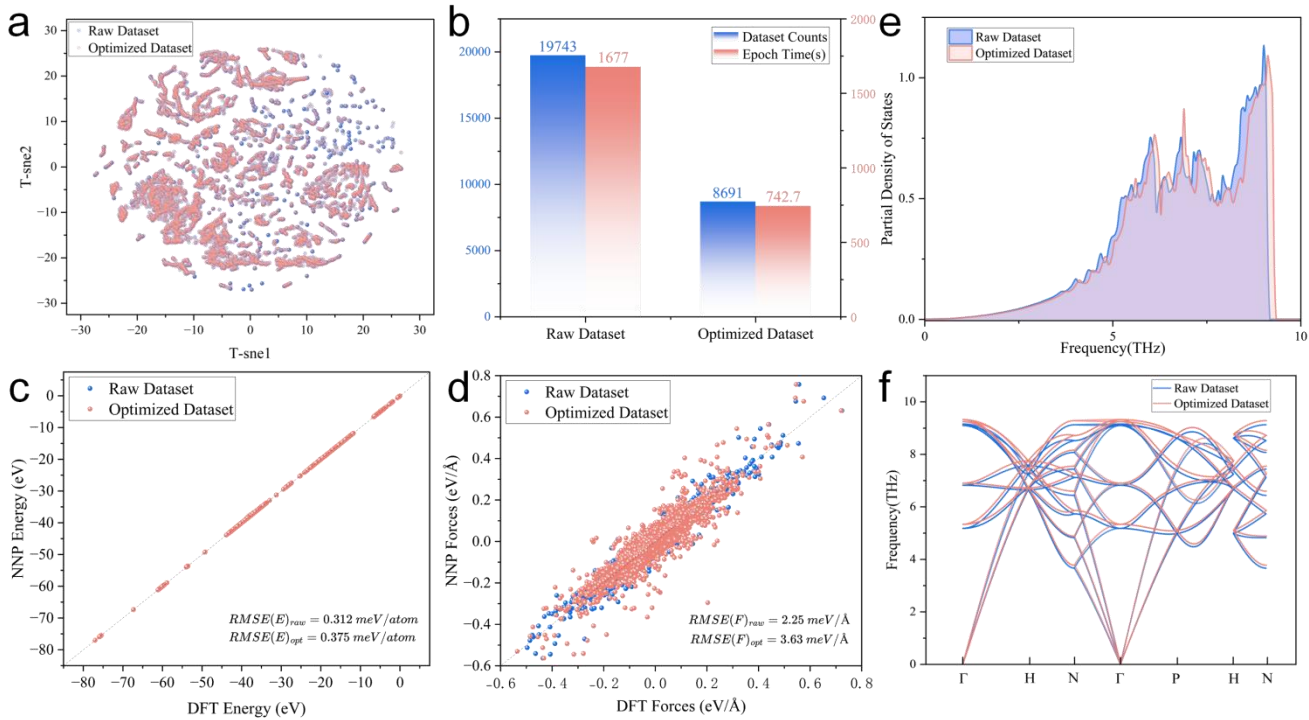


**Figure 3**(a) t-SNE visualization of structural similarities in the  $\alpha$ -Fe/H binary system dataset. The blue and red balls represent the original dataset and the optimized dataset, respectively. (b) Average training time per iteration for the original dataset (19,743 structures) versus the optimized dataset (8,691 structures). (c & d) Comparison of energy and force prediction errors: For the full dataset, the energy RMSE is 0.312 meV/atom and the force RMSE is 2.25 meV/Å. For the optimized dataset, the energy RMSE increases to 0.375 meV/atom, and the force RMSE rises to 3.63 meV/Å. (e & f) Phonon spectrum and band diagram comparison: The phonon spectrum and band diagram generated using the potential function trained on the full dataset show strong consistency with those produced from the optimized dataset, indicating the preservation of key physical trends.

To investigate the generalizability of our method, we further utilized the raw dataset of the  $\alpha$ -Fe/H dual system provided by literature<sup>42</sup>, which contains 19,743 structural configurations. As demonstrated in **Figure 3a**, the use of t-SNE technology for dimensionality reduction and visualization of difference vectors reveals that structures mapped in different colors are densely clustered, indicating a high degree of similarity among

numerous structures in expressing the diversity of the system, thereby highlighting significant data redundancy. Based on this observation, employing the aforementioned data optimization strategy, we refined the dataset to 8,691 structures, achieving a redundancy reduction of up to 55.98%. Leveraging the outcomes of the visualization, we conducted a targeted data screening. As a result, we established an optimized subset comprising 8,691 structures, indicating a reduction in data volume by approximately 56.46%. Figure 2b illustrates the comparison of the average training time per iteration between the original and optimized datasets. The average training time per iteration decreased from 1,677 seconds to 742.7 seconds, resulting in an impressive 55.8% reduction in time cost per iteration. This optimization significantly reduced the expenses incurred during the training process.

Based on the t-SNE dimensionality reduction visualization of the dataset's difference vectors, the same color represents the same chemical formula. The performance of the machine learning potential function on the test set is depicted in **Figure 3c** and **Figure 3d**. With the full dataset, the root mean square error (RMSE) for energy prediction is 0.312 meV/atom, and for force prediction, it is 2.25 meV/Å. However, when the model is trained on the optimized dataset, the RMSE for energy prediction increases to 0.375 meV/atom, and for force prediction, it rises to 3.63 meV/Å.

**Figure 3e** and **Figure 3f** show the phonon spectrum and band diagram generated using the potential function trained on both the raw dataset and the optimized dataset. The trends exhibited in both figures reveal a high degree of consistency, indicating that the optimization process has not significantly altered the underlying physical properties represented by the phonons. This suggests that the optimization technique employed is effective at preserving essential features while potentially improving computational efficiency and accuracy. The phonon spectra in both figures reflect similar peaks and overall patterns, demonstrating that the critical vibrational characteristics of the material remain intact despite the reduction in dataset size. This consistency reinforces the notion that the machine learning potential function maintains its reliability and robustness across varying datasets.

Properties		OPT	DFT	REF	ALL
Lattice constants (Å)	$a_0$	2.83	2.83	2.83	2.83
Vacancy formation energy	<i>monovacancy</i>	2.31	2.223	2.2	2.3
Elastic constants (GPa)	$C_{11}, C_{12}, C_{14}$	290.2 ,147.8,92.8	296 ,151 ,105	296 ,147 ,96	270.1 ,120.3,90.2

**Table 1: Comparison of Potential Function Properties for the Fe-H System.**

**Table 1** presents a comparative analysis of the potential function properties for the Fe-H system. We

compared the properties obtained from the potential function trained with the optimized dataset (OPT) against those trained with the raw dataset, calculated via DFT, and obtained from the reference literature (REF)<sup>43</sup>. Specifically, OPT represents the properties calculated from the potential function trained with the optimized dataset using the method presented in this paper, DFT denotes the properties derived from first-principles calculations, and REF indicates the properties calculated from the potential function trained by the authors of the reference literature. To avoid issues arising from training configurations, we also established a set labeled ALL, which represents the properties calculated from the potential function trained with the full dataset under the same configuration. The results show that the lattice constants provided by OPT, ALL, DFT, and REF are identical, at 2.83 Å, indicating that the results are consistent whether obtained through training with the optimized dataset, the full dataset, or via first-principles calculations. In terms of vacancy formation energy, there are slight differences among the values provided by OPT, ALL, DFT, and REF, but all fall within the range of 2.2 to 2.31, with overall small discrepancies. Regarding the elastic constants C11, C12, and C14, there are some differences between the results given by OPT and those by DFT and REF, but the results of OPT and ALL are relatively close to each other. This suggests that under the same training configuration, the optimized model demonstrates a high degree of consistency in describing the elastic behavior of the Fe-H system.

## 2.5 Comparison of SOAP and DV-LAE Methods for Data Screening and Prediction Accuracy

In literature <sup>42</sup>, a SOAP descriptor-based similarity calculation method was proposed for data screening. Specifically, the atomic descriptors of the candidate structures and those in the training set were calculated using smooth overlap of atomic positions (SOAP) descriptors. SOAP descriptors effectively capture the high-dimensional representations of atomic environments, providing a robust tool for similarity assessment. The steps of the similarity calculation are as follows:

- i) For each candidate structure, we calculate the representation vector of its atomic environment using SOAP descriptors.
- ii) Similarly, SOAP descriptors are calculated for every structure in the training set.
- iii) The Euclidean distance is then used to compute the similarity between the descriptors of candidate structures and those in the training set. Specifically, for each descriptor in the training set, the minimum Euclidean distance to the candidate structure 's descriptor is taken as the measure of similarity.
- iv) Based on these similarity values, the maximum similarity and the average similarity are computed to assess how well the candidate structure represents the training set as a whole.

During the data screening process, a similarity threshold was set. If the average similarity of a candidate structure exceeds this threshold, it is deemed sufficiently representative of the atomic environments in the training set and is included in the training data. This method allows for low-cost data screening without the need for expensive DFT calculations, as only structural information is required to compute SOAP descriptors and similarity scores. However, as the size of the training data increases, the computational cost of this method also rises significantly.

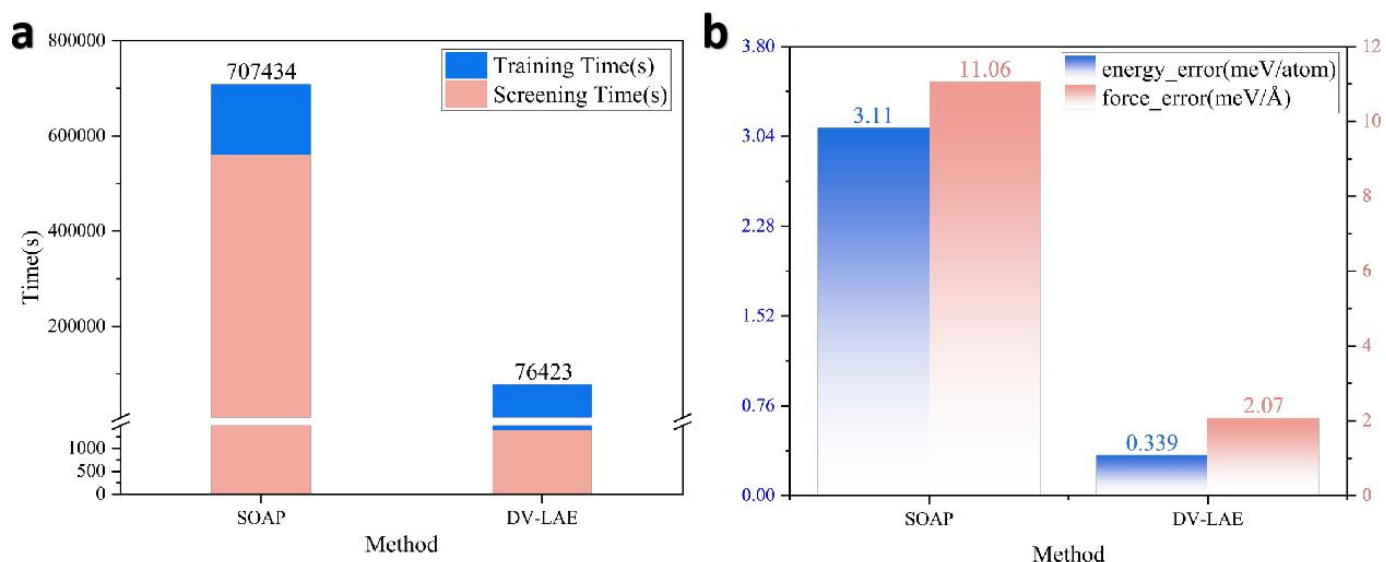


**Figure 4:** (a) Total Time Comparison between the SOAP and DV-LAE methods. Blue represents screening time, while pink indicates training time. (b) Error Comparison showing both energy error (in blue) and force error (in pink) for the SOAP and DV-LAE methods.

To compare our approach with the SOAP and DV-LAE methods, we applied both methods to the Fe-H dataset, which initially contained 19,743 structures. Using the SOAP descriptor method with a threshold of 0.1, data screening was completed in 562,185 seconds, resulting in an optimized dataset containing 17,900 structures. This dataset was then used to train a potential function over 100 iterations, with an average training time of 1,452 seconds per iteration. **Figure 4a** clearly shows the significant time difference between the two methods. The total time for the SOAP method is represented in blue and pink bars, with the blue portion indicating screening time and the pink portion representing training time. The SOAP method not only took longer for screening but also for training, with the total time approaching 707,434 seconds.

In contrast, using our method (DV-LAE), the data screening process on the same dataset resulted in an optimized subset of 8,691 structures, completed in significantly less time. As shown in **Figure 4a**, our method exhibits a drastically reduced time for both screening and training, with a total of 75,423 seconds. The same training configuration of 100 iterations was employed, but the average time per iteration was reduced to 750 seconds, representing a considerable improvement in efficiency compared to the SOAP

method.

For accuracy, the test set results showed that with the SOAP method, the energy error was 3.11 meV/atom, and the force error was 11.06 meV/Å. However, with our method, the energy error decreased to 0.339 meV/atom, and the force error dropped to 2.07 meV/Å. These improvements in predictive accuracy are depicted in **Figure 4b**, where our method ("DV-LAE") significantly outperforms the SOAP method, as indicated by the lower error bars for both energy and force predictions.

In summary, while the SOAP descriptor-based method effectively reduces the data size and improves training efficiency, **Figure 4** clearly demonstrates that our approach not only provides a more efficient data screening process but also yields much better predictive accuracy in both energy and force calculations.

## 2.6 Comparison of SOAP and DV-LAE Methods for Data Screening and Prediction Accuracy

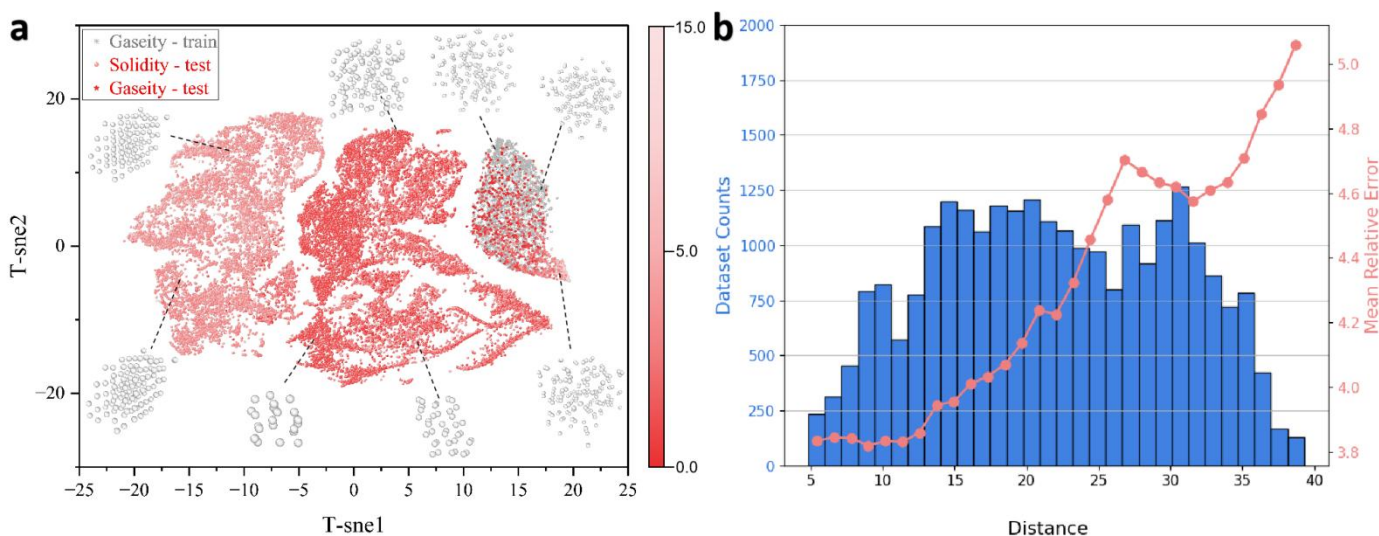


**Figure 5** (a) t-SNE visualization using the DV-LAE method, where gray represents gaseous hydrogen from the training set, red stars represent gaseous hydrogen from the test set, and red circles represent solid hydrogen from the test set. The color intensity reflects the relative energy error, with darker red indicating lower error. (b) Histogram showing the number of test points at different distances from the training set (blue bars) and the corresponding mean relative error (red line).

As shown in **Figure 5a** presents the t-SNE visualization of the difference vector calculated using our method, DV-LAE, where the potential function was trained with gaseous hydrogen and tested with both gaseous and solid hydrogen. Different colors represent the distinction between the training and test datasets: gray represents gaseous hydrogen in the training set, red (star-shaped) indicates gaseous hydrogen in the test set, and red (circle-shaped) represents solid hydrogen in the test set. The color intensity corresponds to the relative energy error, with deeper red indicating lower error and lighter shades representing higher error. It is evident that the test set is distributed with significant clustering differences from the training set in the difference vector space. Test points for gaseous hydrogen are closely clustered near the gaseous hydrogen

training set, with slightly higher errors appearing in points further from the training cluster. This is particularly clear in the distribution of solid hydrogen, which exhibits larger deviations.

**Figure 5b** illustrates the relationship between the distance of test points from the center of the training dataset and their respective relative errors. The blue histogram represents the number of test points within different distance ranges, while the red curve indicates the mean relative error within each range. As the distance from the training set increases, the average relative error also increases, indicating that the further a test point is from the training set in feature space, the greater the prediction error. This highlights the effectiveness of our DV-LAE method in quantifying and visualizing the divergence between training and test data distributions.

Utilizing the DV-LAE technique facilitates the effective visualization of the spatial positioning of novel data in relation to the original dataset. This visualization offers an intuitive means to assess the alignment of these new data points with the established training data. The identification of new structures that are distant from the training data within the difference vector space may serve as an indicator of their “out-of-distribution” status, suggesting potential unreliability for accurate predictions by the trained model.

This concept is in agreement with the findings presented by Zhang et al.<sup>44</sup> who investigate the challenges associated with out-of-distribution (OOD) data. Their study highlights that model performance is typically compromised on OOD data, as these data points exist outside the scope of the training distribution, thereby diminishing their reliability for prediction tasks. The application of this method in practical scenarios enables researchers to dynamically evaluate the trustworthiness of predictions for new, unseen data points. This evaluation process can pinpoint areas within simulations that may necessitate further investigation or additional training to improve the model’s robustness and accuracy in accommodating a variety of structural variations.

Furthermore, the DV-LAE method provides a framework for assessing the rationality of newly simulated structures. When the difference vectors of these structures fall within the bounds of the training data, it suggests a high degree of similarity with the original dataset, indicating a higher likelihood of reliable predictions. Conversely, if the new structures are positioned at the periphery of the difference vector space or are significantly removed from the training data, they may be classified as “out-of-distribution,” which could result in reduced prediction accuracy.

Therefore, the DV-LAE method not only offers an intuitive visualization tool for new structures but also serves as a critical instrument for evaluating their rationality and credibility. This functionality empowers researchers to undertake a more rigorous analysis of new structures during simulations, thereby enhancing the comprehension of potential material behaviors and properties.

## Summary

In summary, the study utilized Ab Initio Molecular Dynamics (AIMD) trajectories and t-SNE visualizations to analyze atomic configurations and data redundancy. Through targeted data screening, the researchers

successfully reduced data volume and training times while maintaining prediction accuracy.

For the high-temperature, high-pressure hydrogen system, an optimized dataset was created, resulting in a 31.79% reduction in data volume and a 41.4% decrease in average training time per iteration. The optimized dataset maintained comparable accuracy to the original, with only slight increases in Root Mean Square Error (RMSE) for energy and force predictions.

The  $\alpha$ -Fe/H binary system dataset was also optimized, reducing data volume by 55.98% and training time by 55.8%. Despite increased RMSE values for energy and force predictions, the optimized dataset preserved key physical trends, as evidenced by consistent phonon spectra and band diagrams.

A comparison between the SOAP and DV-LAE methods for data screening revealed that the DV-LAE method not only reduced screening and training times significantly but also improved prediction accuracy. The DV-LAE method also provided a visualization tool to assess the rationality of newly simulated structures, identifying "out-of-distribution" data points that may compromise model performance.

Overall, the study demonstrated the effectiveness of data optimization techniques in enhancing computational efficiency and accuracy in materials science applications, while also providing valuable insights into the relationships between various atomic configurations. The DV-LAE method emerged as a powerful tool for data screening and model evaluation, offering researchers a means to dynamically assess the trustworthiness of predictions for new, unseen data points.

## Methods

Firstly, select a reference structure that includes all the elemental types of the target system as the benchmark, ensuring that the reference structure can fully represent all elemental combinations and interactions of the target system. Doing so provides a standardized environment for the atomic interactions between different elements, and the feature vectors derived from this reference structure can accurately reflect the differences in the local environment of the system, thereby providing a comprehensive basis for comparing and analyzing other structures. Subsequently, use atomic environment descriptors to characterize the local environmental features within the structure. These descriptors include radial symmetry functions (Equation 1) and angular symmetry functions (Equations 2 and 3), which can delicately describe the local environment of the system.<sup>45,46</sup> Equation 4 is a cutoff function that controls the range of the local environment covered by the aforementioned symmetry functions based on the given cutoff radius.

$$G_i^2 = \sum_j e^{-\eta(R_{ij}-R_s)^2} \cdot f_c(R_{ij}) \quad (1)$$

$$G_i^4 = 2^{1-\xi} \sum_{j,k \neq i}^{all} (1 + \lambda \cos \theta_{ijk})^\xi \cdot e^{-\eta(R_{ij}^2 + R_{ik}^2 + R_{jk}^2)} \cdot f_c(R_{ij}) \cdot f_c(R_{ik}) \cdot f_c(R_{jk}) \quad (2)$$

$$G_i^5 = 2^{1-\xi} \sum_{j,k \neq i}^{all} (1 + \lambda \cos \theta_{ijk})^\xi \cdot e^{-\eta(R_{ij}^2 + R_{ik}^2)} \cdot f_c(R_{ij}) \cdot f_c(R_{ik}) \quad (3)$$

$$f_c(r) = \begin{cases} 1, & \text{for } 0 \leq r < r_{ci} \\ f(x), & \text{for } r_{ci} \leq r < r_c \text{ where } x = \frac{r - r_{ci}}{r_c - r_{ci}} \\ 0 & \text{for } r \geq r_c \end{cases} \quad (4)$$

Machine learning potential functions rely on these descriptors to predict the contribution of each atomic pair to the total energy of the system, thereby summing up to obtain the total energy of the system. Thus, these descriptors have a significant impact on the accuracy of the machine learning potential functions. By setting different parameter configurations, we can obtain various combinations of descriptors that reflect the diversity of the local environment of the system. However, since a single descriptor only describes the local environment, to differentiate between different systems, we need to consider the values of all descriptors for each structure comprehensively.

To effectively capture the differences between structures, we employ histogram statistics to tally occurrences within each descriptor value interval. Inspired by the "less is more" concept highlighted in literature <sup>47</sup>, our approach emphasizes the presence of values across intervals rather than their exact quantities, allowing for the efficient representation of structural features even with smaller training sets.

In the construction of difference vectors, we leverage a binary representation to identify disparities between the histogram intervals of descriptors in the current structure and those in a reference structure. This comparison is encapsulated by a binary function that flags differences, utilizing the XOR operation to yield a binary outcome where '1' signifies a difference and '0' indicates similarity.

The generation of the difference vector  $D$  is conducted through a systematic process that leverages histogram statistics and binary comparison to encapsulate the disparities between the current structure and a reference structure across various descriptors  $G_i$ . The procedure is as follows:

- i) **Histogram Construction:** For each descriptor  $G_i$  of the current and reference structures, construct histograms by binning the values into a predefined number of intervals,  $N$ . Let  $H_{current,j}$  and  $H_{ref,j}$  represent the histogram bins for the current and reference structures, respectively, where  $j$  denotes the interval index.

- ii) **Binary Comparison via XOR Operation:** For each interval  $j$ , apply the XOR operation to the corresponding histogram bin counts to identify differences:

$$d_{i,j} = H_{current,j} \oplus H_{ref,j} \quad (5)$$

Here,  $d_{i,j}$  is a binary variable where '0' indicates no difference (both bins have the same count) and '1' signifies a difference (bins have distinct counts).

- iii) **Aggregation of Descriptor Differences:** For each descriptor  $G_i$ , aggregate the binary differences  $d_{i,j}$  across all intervals to form a descriptor-specific difference vector  $\vec{d}_i$ :

$$\vec{d}_i = [d_{i,1}, d_{i,2}, \dots, d_{i,N}] \quad (6)$$

- iv) **Formation of the Comprehensive Difference Vector:** Concatenate the descriptor-specific difference vectors  $\vec{d}_i$  for all descriptors  $G_i$  in the system to create the comprehensive difference vector  $D$ :

$$D = [\vec{d}_1, \vec{d}_2, \dots, \vec{d}_m] \quad (7)$$

where  $m$  is the total number of descriptors.

This difference vector  $D$  serves as a compact representation that captures the relative differences between structures. By applying dimensionality reduction techniques such as t-SNE, we can visually represent these differences, facilitating a better understanding of structural variations.<sup>48,49</sup>

Ultimately, by strategically selecting a subset of data that reflects this difference vector analysis, we can curate a dataset that minimizes redundancy while preserving diversity. This refined dataset serves as a high-quality input for training machine learning potential functions, enhancing the efficiency and accuracy of our models without compromising on the breadth of structural representation.

### Code Availability

For readers' convenience, the codes are available via: <https://github.com/Weijie-Yang/DV-LAE>.

### Conflict of Interests

There is no conflict of interests to declare.

### Reference

1. Engel, E. *Density Functional Theory*. (Springer, 2011).
2. Sholl, D. S. & Steckel, J. A. *Density Functional Theory: A Practical Introduction*. (John Wiley & Sons, 2022).
3. Jones, R. O. Density functional theory: Its origins, rise to prominence, and future. *Reviews of modern*

*physics* **87**, 897 (2015).

4. Marx, D. & Hutter, J. *Ab Initio Molecular Dynamics: Basic Theory and Advanced Methods*. (Cambridge University Press, 2009).
5. Wu, X., Kang, F., Duan, W. & Li, J. Density functional theory calculations: A powerful tool to simulate and design high-performance energy storage and conversion materials. *Progress in Natural Science: Materials International* **29**, 247–255 (2019).
6. Pan, J. Scaling up system size in materials simulation. *Nature Computational Science* **1**, 95–95 (2021).
7. Burke, K. Perspective on density functional theory. *The Journal of chemical physics* **136**, (2012).
8. Rupp, M., Ramakrishnan, R. & Von Lilienfeld, O. A. Machine learning for quantum mechanical properties of atoms in molecules. *The Journal of Physical Chemistry Letters* **6**, 3309–3313 (2015).
9. Ramprasad, R., Batra, R., Pilania, G., Mannodi-Kanakkithodi, A. & Kim, C. Machine learning in materials informatics: recent applications and prospects. *npj Computational Materials* **3**, 54 (2017).
10. Poltavsky, I. & Tkatchenko, A. Machine learning force fields: Recent advances and remaining challenges. *The journal of physical chemistry letters* **12**, 6551–6564 (2021).
11. Unke, O. T. *et al.* Machine learning force fields. *Chemical Reviews* **121**, 10142–10186 (2021).
12. Gubernatis, J. E. & Lookman, T. Machine learning in materials design and discovery: Examples from the present and suggestions for the future. *Physical Review Materials* **2**, 120301 (2018).
13. Mailoa, J. P. *et al.* A fast neural network approach for direct covariant forces prediction in complex multi-element extended systems. *Nat Mach Intell* **1**, 471–479 (2019).
14. Behler, J. Perspective: Machine learning potentials for atomistic simulations. *The Journal of Chemical Physics* **145**, 170901 (2016).
15. Bartók, A. P., Kermode, J., Bernstein, N. & Csányi, G. Machine learning a general-purpose interatomic potential for silicon. *Physical Review X* **8**, 041048 (2018).
16. Deringer, V. L. & Csányi, G. Machine learning based interatomic potential for amorphous carbon. *Physical Review B* **95**, 094203 (2017).
17. Behler, J. & Parrinello, M. Generalized Neural-Network Representation of High-Dimensional Potential-Energy Surfaces. *Phys. Rev. Lett.* **98**, 146401 (2007).
18. Behler, J. & Parrinello, M. Generalized neural-network representation of high-dimensional potential-energy surfaces. *Physical review letters* **98**, 146401 (2007).
19. Zhang, L., Han, J., Wang, H., Car, R. & E, W. Deep potential molecular dynamics: a scalable model with the accuracy of quantum mechanics. *Physical review letters* **120**, 143001 (2018).
20. Han, J., Zhang, L., Car, R., & others. Deep potential: A general representation of a many-body potential energy surface. *arXiv preprint arXiv:1707.01478* (2017).
21. Smith, J. S., Isayev, O. & Roitberg, A. E. ANI-1: an extensible neural network potential with DFT accuracy at force field computational cost. *Chemical science* **8**, 3192–3203 (2017).
22. Schütt, K. T., Sauceda, H. E., Kindermans, P.-J., Tkatchenko, A. & Müller, K.-R. SchNet – A deep learning architecture for molecules and materials. *The Journal of Chemical Physics* **148**, 241722 (2018).
23. Park, C. W. *et al.* Accurate and scalable graph neural network force field and molecular dynamics with direct force architecture. *Npj Comput Mater* **7**, 73 (2021).
24. Zhou, L., Pan, S., Wang, J. & Vasilakos, A. V. Machine learning on big data: Opportunities and challenges. *Neurocomputing* **237**, 350–361 (2017).
25. Jordan, M. I. & Mitchell, T. M. Machine learning: Trends, perspectives, and prospects. *Science* **349**, 255–260 (2015).
26. Wei, J. *et al.* Machine learning in materials science. *InfoMat* **1**, 338–358 (2019).
27. Chen, J. The development and comparison of molecular dynamics simulation and Monte Carlo simulation. in *IOP Conference Series: Earth and Environmental Science* vol. 128 012110 (IOP Publishing, 2018).
28. Okamoto, Y. Generalized-ensemble algorithms: enhanced sampling techniques for Monte Carlo and molecular dynamics simulations. *Journal of Molecular Graphics and Modelling* **22**, 425–439 (2004).

29. Binder, K. *Monte Carlo and Molecular Dynamics Simulations in Polymer Science*. (Oxford University Press, 1995).
30. Jorgensen, W. L. & Tirado-Rives, J. Monte Carlo vs molecular dynamics for conformational sampling. *The Journal of Physical Chemistry* **100**, 14508–14513 (1996).
31. Wood, W. W. & Erpenbeck, J. J. Molecular dynamics and Monte Carlo calculations in statistical mechanics. *Annual Review of Physical Chemistry* **27**, 319–348 (1976).
32. Paquet, E. & Viktor, H. L. Molecular dynamics, monte carlo simulations, and langevin dynamics: a computational review. *BioMed research international* **2015**, (2015).
33. Rupakheti, C., Virshup, A., Yang, W. & Beratan, D. N. Strategy To Discover Diverse Optimal Molecules in the Small Molecule Universe. *J. Chem. Inf. Model.* **55**, 529–537 (2015).
34. Gražulis, S. *et al.* Crystallography Open Database (COD): an open-access collection of crystal structures and platform for world-wide collaboration. *Nucleic acids research* **40**, D420–D427 (2012).
35. Jain, A. *et al.* Commentary: The Materials Project: A materials genome approach to accelerating materials innovation. *APL materials* **1**, (2013).
36. Saal, J. E., Kirklin, S., Aykol, M., Meredig, B. & Wolverton, C. Materials design and discovery with high-throughput density functional theory: the open quantum materials database (OQMD). *Jom* **65**, 1501–1509 (2013).
37. Mu, S. *et al.* Uncovering electron scattering mechanisms in NiFeCoCrMn derived concentrated solid solution and high entropy alloys. *npj Computational Materials* **5**, 1 (2019).
38. Bowman, J. M. *et al.* The MD17 datasets from the perspective of datasets for gas-phase “small” molecule potentials. *J. Chem. Phys.* **156**, 240901 (2022).
39. Zhang, Y. *et al.* DP-GEN: A concurrent learning platform for the generation of reliable deep learning based potential energy models. *Comput Phys Commun* **253**, 107206 (2020).
40. Zhang, L., Lin, D.-Y., Wang, H., Car, R. & E, W. Active learning of uniformly accurate interatomic potentials for materials simulation. *Physical Review Materials* **3**, 023804 (2019).
41. Cheng, B., Mazzola, G., Pickard, C. J. & Ceriotti, M. Evidence for supercritical behaviour of high-pressure liquid hydrogen. *Nature* **585**, 217–220 (2020).
42. Meng, F.-S. *et al.* General-purpose neural network interatomic potential for the  $\alpha$ -iron and hydrogen binary system: Toward atomic-scale understanding of hydrogen embrittlement. *Physical Review Materials* **5**, 113606 (2021).
43. Zhang, S., Meng, F., Fu, R. & Ogata, S. Highly efficient and transferable interatomic potentials for  $\alpha$ -iron and  $\alpha$ -iron/hydrogen binary systems using deep neural networks. *Computational Materials Science* **235**, 112843 (2024).
44. Omeo, S. S., Fu, N., Dong, R., Hu, M. & Hu, J. Structure-based out-of-distribution (OOD) materials property prediction: a benchmark study. *npj Comput Mater* **10**, 144 (2024).
45. Behler, J. & Parrinello, M. Generalized Neural-Network Representation of High-Dimensional Potential-Energy Surfaces. *Phys. Rev. Lett.* **98**, 146401 (2007).
46. Behler, J. Atom-centered symmetry functions for constructing high-dimensional neural network potentials. *The Journal of Chemical Physics* **134**, 074106 (2011).
47. Smith, J. S., Nebgen, B., Lubbers, N., Isayev, O. & Roitberg, A. E. Less is more: Sampling chemical space with active learning. *J. Chem. Phys.* **148**, 241733 (2018).
48. Van der Maaten, L. & Hinton, G. Visualizing data using t-SNE. *Journal of machine learning research* **9**, (2008).
49. Wattenberg, M., Viégas, F. & Johnson, I. How to use t-SNE effectively. *Distill* **1**, e2 (2016).